ARTICLE IN PRESS

Nature Communications

https://doi.org/10.1038/s41467-026-70324-3

Article in Press

Metal-organic framework-confined Co_3O_4 for humidity-immune ozone decomposition

Received: 15 September 2025

Accepted: 23 February 2026

Cite this article as: Lou, Y., Han, Y., Li, T. *et al.* Metal-organic framework-confined Co_3O_4 for humidity-immune ozone decomposition. *Nat Commun* (2026). https://doi.org/10.1038/s41467-026-70324-3

Yuning Lou, Yuejiang Han, Tianshuo Li, Zhi-Ming Zhang & Zhengbo Han

We are providing an unedited version of this manuscript to give early access to its findings. Before final publication, the manuscript will undergo further editing. Please note there may be errors present which affect the content, and all legal disclaimers apply.

If this paper is publishing under a Transparent Peer Review model then Peer Review reports will publish with the final article.

ARTICLE IN PRESS

© The Author(s) 2026. **Open Access** This article is licensed under a Creative Commons Attribution-NonCommercial-NoDerivatives 4.0 International License, which permits any non-commercial use, sharing, distribution and reproduction in any medium or format, as long as you give appropriate credit to the original author(s) and the source, provide a link to the Creative Commons licence, and indicate if you modified the licensed material. You do not have permission under this licence to share adapted material derived from this article or parts of it. The images or other third party material in this article are included in the article's Creative Commons licence, unless indicated otherwise in a credit line to the material. If material is not included in the article's Creative Commons licence and your intended use is not permitted by statutory regulation or exceeds the permitted use, you will need to obtain permission directly from the copyright holder. To view a copy of this licence, visit http://creativecommons.org/licenses/by-nc-nd/4.0/.

ARTICLE IN PRESS

Metal-organic framework-confined Co_3O_4 for humidity-immune ozone decomposition

Yuning Lou[1], Yuejiang Han[1], Tianshuo Li[1], Zhi-Ming Zhang[2] & Zhengbo Han[1,*]

[1] College of Chemistry, Liaoning University, Shenyang 110036, P. R. China.

[2] Institute for New Energy Materials and Low Carbon Technologies, School of Materials Science and Engineering, Tianjin University of Technology, Tianjin 300384 P. R. China.

[*] Corresponding authors

E-mail: ceshzb@lnu.edu.cn (Z. H)

ARTICLE IN PRESS

ARTICLE IN PRESS

Abstract

Ground-level ozone (O_3) is a major air pollutant, and catalytic decomposition represents a promising strategy for its removal. However, maintaining high catalytic efficiency under humid conditions remains a considerable challenge. In this study, we encapsulate ultrafine metal oxides (UMOs; e.g., Co_3O_4, NiO) within the nanopores of an Fe_3O-cluster-based metal–organic framework, PCN-333(Fe), for catalytic O_3 decomposition. The optimized 30% Co_3O_4@PCN-333(Fe) catalyst achieves sustained 100% O_3 conversion for over 120 hours in a continuous airflow containing 40 ppm O_3 under high space velocity (1.75×10^5 h^{-1}) and a broad range of humidity (10-90% RH). Mechanistic investigations reveal that the exceptional performance originates from an interfacial hydrogen-atom transfer process between Co_3O_4 and the Fe_3O clusters of PCN-333(Fe), as confirmed by in situ diffuse reflectance infrared Fourier-transform spectroscopy (DRIFTS) and in situ Raman spectroscopy. This work proposes a general principle for designing humidity-immune catalytic interfaces between metal oxides and porous materials, thereby providing a practical foundation for sustainable control of pollutant emissions in complex environments.

ARTICLE IN PRESS

Introduction

Ground-level ozone (O_3) has emerged as a major global air pollutant, posing serious threats to both environmental quality and public health[1, 2]. Outdoor O_3 is primarily generated through photochemical reactions between nitrogen oxides and volatile organic compounds under sunlight, while indoor O_3 may accumulate from emissions produced by photocopiers, laser printers, ultraviolet lamps, and disinfection devices[3, 4]. As a potent oxidant, O_3 remains relatively stable at typical ambient concentrations (ppb level)[5]; however, long-term exposure has been associated with respiratory disorders, cardiovascular diseases, and even premature mortality[6, 7]. The World Health Organization has recommended that the 8-h average O_3 concentration exceeding 100 μg m^{-3} (≈ 51 ppb) poses health risks[8]. Alarmingly, O_3 levels exceeding 150 ppb are frequently reported in many regions, reflecting severe pollution episodes. These observations underscore the urgent need for efficient, durable, and environmentally sustainable strategies for O_3 removal.

Among various control measures, catalytic decomposition is regarded as the most promising strategy owing to its high efficiency and absence of harmful by-products[9, 10]. Conventional transition-metal oxides exhibit notable activity but suffer from rapid deactivation under humid conditions, where water molecules compete strongly for active sites[11-13]. Dispersing ultrafine metal oxides (UMOs) on carbonaceous or porous substrates can partially alleviate these issues[14], yet such systems still face challenges of weak host–guest interfacial coupling, limited control over particle size, and heterogeneous distributions of active sites. In contrast, metal-organic frameworks (MOFs)

ARTICLE IN PRESS

offer distinct advantages, including tunable organic linkers to balance hydrophilicity/hydrophobicity, robust inorganic nodes to act as active sites, and hierarchical porosity to facilitate mass transport[15-19]. Nevertheless, most reported UMO-MOF composites rely on external loading, which often leads to non-uniform particle distributions, pore blockage, and reduced accessibility of active sites[20-22]. Therefore, designing UMO-MOF catalysts with well-defined structures, strong interfacial interactions, and high stability is of paramount importance, offering new opportunities to overcome current limitations and realize highly efficient O_3 catalytic decomposition.

Herein, we report a series of UMOs@PCN-333(Fe) composites (UMOs = ultrafine Co_3O_4 or NiO nanoparticles), in which the oxide nanoparticles are precisely encapsulated inside the nanopores of PCN-333(Fe) rather than simply deposited on the external surface. Among them, 30% Co_3O_4@PCN-333(Fe) achieves 100% O_3 conversion across a wide humidity (10-90% RH) at room temperature, and maintains long-term stability for over 120 h. DFT calculations combined with in situ spectroscopy reveal that the exceptional catalytic performance originates from interfacial hydrogen-atom transfer between Co_3O_4 and Fe_3O clusters of PCN-333(Fe), which facilitates stepwise O_3 activation, improves O_2 release efficiency, and accelerates active-site regeneration. Furthermore, the remarkable humidity immunity arises from the MOF-confined protection of active sites from water invasion, while water molecules actively participate in the reaction pathway rather than competing with O_3. This work establishes a fundamental principle for engineering interfacial hydrogen-atom transfer within MOF-confined oxide catalysts, thereby providing a

ARTICLE IN PRESS

practical foundation for achieving sustainable pollutant control under complex and variable environmental conditions.

Results

Syntheses and Structural Characterization of UMOs@PCN-333(Fe)

The synthetic route of UMOs@PCN-333(Fe) is depicted in Fig. 1. A sonication-microwave confinement strategy was developed to achieve the precise incorporation of ultrafine metal oxide nanoparticles within the nanopores of PCN-333(Fe). Initially, activated PCN-333(Fe) was dispersed homogeneously in a hydrophobic solvent (e.g. *n*-hexane) by ultrasonication, preventing aggregation and exposing the hierarchical pore system. Subsequently, controlled amounts of UMOs precursors were introduced under 0°C, enabling their gradual penetration into the nanopores of framework. After an aging process that facilitated precursor anchoring, the mixture was carefully filtered and underwent microwave treatment, which induced rapid in situ nucleation and growth of UMOs as highly dispersed clusters confined within the pores of PCN-333(Fe). This step ensured both uniform nanoparticle distribution and preservation of the host crystallinity. Finally, careful purification removed residual reactants without damaging the porous architecture. This synthetic strategy thus provides a versatile platform for embedding nanoscale metal oxides into MOFs, achieving strong interfacial coupling and well-defined hybrid architectures for catalytic applications.

To elucidate the structural characteristics of UMOs@PCN-333(Fe), we selected 30%

ARTICLE IN PRESS

Co_3O_4@PCN-333(Fe) as a representative material. The MTN-type zeolitic topology of PCN-333 (Fig. 1) consists of a dual-mesopore network formed by supertetrahedral building units, with two types of mesocages (4.2 and 5.5 nm in diameter) interconnected by pore windows of ~2.6 and 3.0 nm, thereby providing spatially well-defined compartments for nanoparticle encapsulation[23, 24]. Aberration-corrected high-angle annular dark-field scanning transmission electron microscopy (AC-HAADF-STEM) was employed to probe the structural integrity and encapsulation behavior[25]. The pristine PCN-333(Fe) framework displays periodically arranged mesopores on the (110) plane (Fig. 2a). Upon encapsulation, the 30% Co_3O_4@PCN-333(Fe) sample preserves the parent pore periodicity (Fig. 2b), yet exhibits locally elevated contrast, directly evidencing pore occupation by Co_3O_4 nanoparticles (Fig. 2c). EDS elemental mapping further confirms homogeneous Co distribution across single MOF crystals (Fig. S1). The encapsulated Co_3O_4 nanoparticles exhibit a uniform size of 3.4-3.9 nm (average 3.6 ± 0.1 nm, Fig. S2), which matches the mesoporous cavity dimensions of PCN-333. Scanning Electron Microscope reveals well-retained octahedral morphology with smooth surfaces and absence of surface-deposited aggregates (Fig. S3), corroborating true intracrystalline encapsulation. These observations unambiguously confirm that Co_3O_4 nanoparticles are formed in situ and precisely confined within the nanopores of PCN-333(Fe), without compromising the structural integrity of its framework.

To probe the chemical state of Co element in 30% Co_3O_4@PCN-333(Fe), Co K-edge X-ray absorption near-edge structure (XANES) and extended X-ray absorption fine structure (EXAFS) spectroscopy were performed, revealing an absorption edge between Co foil and bulk Co_3O_4,

ARTICLE IN PRESS

closer to Co_3O_4, indicating a slightly reduced oxidation state due to nanoconfinement-induced interface effects (Fig. 3a)[26]. Fourier-transformed EXAFS (FT-EXAFS, Fig. 3b) reveals a prominent Co-O coordination at ~1.42 Å, marginally shorter than the 1.46 Å path in bulk Co_3O_4[27, 28], while subsequent Co-Co coordination shells are markedly attenuated, directly evidencing the highly dispersed and size-confined nature of the encapsulated clusters. Quantitative EXAFS fitting using crystallographic Co_3O_4 parameters yields excellent agreement (Fig. 3c), unequivocally confirming Co_3O_4 as the dominant crystalline phase while exhibiting subtle oxidation state reduction associated with elevated oxygen vacancy concentrations.

Powder XRD patterns, photograph, and FT-IR spectra (Fig. 3d and Figs. S4-S5) confirm the preservation of PCN-333(Fe)'s crystalline integrity following Co_3O_4 incorporation across various loadings. The absence of distinct Co_3O_4 diffraction peaks precludes large particle formation, instead indicating highly dispersed, ultra-small Co_3O_4 nanoclusters[29, 30]. Raman spectroscopy identifies the characteristic Co_3O_4 peak at 682 cm^{-1} (Fig. 3e), confirming the encapsulated phase's identity as Co_3O_4[31, 32]. N_2 adsorption isotherms (Fig. 3f) and pore size analysis (Fig. S6) reveal a systematic decrease in uptake capacity with increasing Co_3O_4 loading, consistent with progressive pore filling. Notably, unlike previous reports where metal oxides (e.g., TiO_2) were confined solely to mesopores, Co_3O_4 in this work also occupies micropores (~11 Å diameter), attributable to the smaller size of its precursors[25]. Inductively coupled plasma optical emission spectrometry (ICP-OES) quantitatively verifies Co_3O_4 mass percentages of 9.4%, 18.6%, and 27.3% (Table S1), aligning with the designated loadings. Similarly, structure characterization of NiO (Figs. S7-S10)

ARTICLE IN PRESS

confirms its successful encapsulation within the PCN-333(Fe) framework.

O_3 catalytic decomposition on UMOs@PCN-333(Fe)

The O_3 catalytic decomposition performance of UMOs@PCN-333(Fe) was evaluated with a dynamic test at various humidity and temperature on a custom-built ozone analyzer at an inlet O_3 concentration of 40 ppm (Fig. S11). The effect of varying oxide loadings on catalyst under low (10% RH) and high humidity (90% RH) conditions was first optimized (Figs. S12-S13). Remarkably, 30% Co_3O_4@PCN-333(Fe) maintains complete O_3 conversion for more than 160 h at 40°C even under 10% RH (Fig. 4a), attesting to its outstanding durability in dry environments, with a performance level comparable to the best catalysts reported to date[13, 33-36]. In addition, the catalytic rate of O_3 decomposition over 30% Co_3O_4@PCN-333(Fe) was calculated to be 1.9 $mmol \cdot h^{-1} \cdot g_{cat.}^{-1}$. While performance exhibits humidity dependence, degrading to 120 hours at 90% RH, this still represents exceptional longevity under high moisture stress compared to benchmark materials. Furthermore, a pronounced positive temperature dependence of catalytic stability at fixed low humidity (10% RH): 30% Co_3O_4@PCN-333(Fe) sustains 100% O_3 conversion for 50 hours even at a low temperature of 10°C, underscoring its exceptional intrinsic activity and robustness in O_3 catalytic decomposition (Fig. 4b). Under 10% RH (Fig. 4c), the O_3 conversion of bulk Co_3O_4 and pristine PCN-333(Fe) rapidly deactivate, reaching peak conversions of <10% and <30% within 3 h, far below the sustained 100% activity of the composite. Even at 90% RH, 30% Co_3O_4@PCN-333(Fe) preserves its pronounced advantage, underscoring its superior humidity

ARTICLE IN PRESS

immunity (Fig. 4d). These results highlight the synergistic catalysis arising from the MOF-encapsulated UMOs structure.

The robustness of 30% Co_3O_4@PCN-333(Fe) to dynamic environmental fluctuations is shown in Figs 4e-f. When subjected to fluctuating humidity cycles between 30% and 90% RH, or temperature shifts between 10°C and 40°C, the material consistently maintains 100% O_3 conversion for 50+ hours without performance decay. This robust adaptability underscores its capability to handle real-world atmospheric variability where humidity and temperature rarely remain static. Optimization of the active phase loading is critical for maximizing humidity immunity. Fig. 4g demonstrates that Co_3O_4@PCN-333(Fe) with 10% loading sustains 100% conversion for only 20 hours at 90% RH, whereas increasing the loading to 30% extends this duration to more than 160 hours. This pronounced Co_3O_4 loading dependence unequivocally demonstrates that achieving an optimal Co_3O_4 density within the PCN-333(Fe) framework is indispensable for preserving abundant and accessible catalytic sites, particularly under wet environments.

Critically, 30% Co_3O_4@PCN-333(Fe) exhibits industry-relevant performance even under simulated extreme environments, underscoring its substantial potential for practical application. Challenging summertime conditions representative of the Yangtze River Delta region in China, where intense photochemical activity and high humidity converge to produce severe O_3 pollution episodes, thereby underscoring the urgent necessity of effective removal strategies. Remarkably, under these accelerated degradation conditions, 30% Co_3O_4@PCN-333(Fe) sustains complete O_3

ARTICLE IN PRESS

decomposition for 120 hours (Fig. 4h). This superior stability highlights not only the high intrinsic activity of the encapsulated architecture but also its resilience against the simultaneous thermal and humidity stresses that typically deactivate conventional catalysts. Beyond the single Co_3O_4 system, the encapsulation strategy proves broadly generalizable for enhancing the catalytic efficiency of diverse transition metal oxides. As demonstrated in Fig. 4i, PCN-333(Fe) incorporating NiO, or Co_3O_4 nanoclusters achieves over 120 hours of continuous and complete O_3 conversion under optimized conditions, markedly outperforming state-of-the-art benchmarks (Table S2). Furthermore, systematic evaluations of NiO@PCN-333(Fe) a (Figs. S14-S16) confirm its outstanding decomposition activity across a wide range of environmental conditions. Although all encapsulated composites deliver transformative stability enhancements relative to their bulk oxide counterparts, 30% Co_3O_4@PCN-333(Fe) consistently demonstrates the highest activity-to-stability balance, firmly establishing it as a leading candidate for scalable and durable industrial O_3 removal.

ARTICLE IN PRESS

O_3 Conversion Mechanism over 30% Co_3O_4@PCN-333(Fe)

To elucidate the underlying mechanisms contributing to the excellent O_3 catalytic decomposition performance of 30% Co_3O_4@PCN-333(Fe), X-ray photoelectron spectroscopy (XPS), in situ diffuse reflectance infrared Fourier transform spectroscopy and in situ Raman spectroscopy was performed. The chemical states of both Fe and Co underwent significant changes after the encapsulation of Co_3O_4 particles within the PCN-333(Fe) cages (Fig. 5a-b). Upon Co_3O_4

ARTICLE IN PRESS

encapsulation, the Fe^{2+} content on PCN-333(Fe) increases from 45.1% to 61.9%, while the Co^{2+} content of Co_3O_4 rises from 45.7% to 63.4%. Such concurrent enrichment of reduced Fe and Co species underscores the emergence of an interfacial MOF-UMOs synergistic site, which is directly promoted by the confined architecture. During O_3 decomposition, oxygen vacancies are generated to maintain electrostatic balance, and substantial evidence suggests that these vacancies act as the dominant active sites, accounting for the high catalytic efficiency[12, 37, 38]. This conclusion is corroborated by differential charge density calculation (Fig. S17), which reveals pronounced charge transfer from MOF ligands to Fe and Co centers.

Electron Paramagnetic Resonance (EPR) analysis reveals that O_3 exposure induces $O_2^{\bullet-}$ species in 30% Co_3O_4@PCN-333(Fe) when trapped by DMPO (Fig. S18). The in situ DRIFT spectrum (Fig. 5c) exhibited prominent absorption bands at approximately 3660, 2125, 1650, and 1380 cm^{-1}. These bands are assigned to the O-H stretching vibration of doubly bridged hydroxyl groups (-OHO-)[39], coordinated O_3 complexes adsorbed on Co sites[40], the O-H bending vibrations in adsorbed water and reaction intermediates[41], and peroxide (O_2^{2-}) species[11], respectively. Meanwhile, new peaks were observed in the in situ Raman spectra (Fig. 5d), with the band at 526 cm^{-1} assigned to the O-O stretching vibration in Co-OOH[42-44], and the bands at 804 and 1097 cm^{-1} attributed to O_2^{2-} and O_2^- species[34], respectively, indicating the formation of new intermediates on the catalyst surface during O_3 decomposition. This finding is consistent with the literature reports, suggesting that the peroxide intermediate is active for O_3 catalytic decomposition. Following a 24-hour exposure to an O_3 gas flow, the Raman spectrum of 30% Co_3O_4@PCN-

ARTICLE IN PRESS

333(Fe) showed no significant changes, which suggests that the structural integrity of the catalyst remained intact and undamaged throughout this duration. This observation serves to confirm the exceptional stability of the material. Furthermore, the accumulation of intermediate products was found to be minimal, and it is noteworthy that the release of these intermediates at the active sites constitutes the rate-limiting step in the O_3 catalytic decomposition process, thereby providing further evidence of the catalyst's outstanding performance.

Density functional theory (DFT) calculations were performed to elucidate the mechanism of O_3 decomposition over Co_3O_4@PCN-333(Fe) (Fig. 6). The model incorporates representative Fe_3O clusters from PCN-333(Fe) and Co_3O_4 nanoclusters to simulate the catalytic interface (Fig. S19). The adsorption sites of H_2O and O_3 in Co_3O_4@PCN-333(Fe) were calculated. H_2O was found to preferentially occupy an open Fe site adjacent to the Co_3O_4, with a distance of 2.223 Å, whereas O_3 was located at a Co site in the vicinity of the Fe_3O cluster, with a distance of 1.825 Å, highlighting the distinct roles of Fe and Co nodes in activating the two adsorbates. Subsequently, the first O_3 molecule preferentially adsorbs onto two adjacent open Co sites, with its two terminal O atoms coordinated to them. Then, the coordinated H_2O at the Fe site dissociates, releasing two free hydrogen atoms. One hydrogen atom reacts with the adsorbed O_3 to generate a Co-OOOH intermediate, while the other is coordinated at the interfacial O atom. The Co-OOOH species then decomposes, releasing the first ·OOOH radical. The second O_3 molecule subsequently adsorbs onto the Co sites, during which the interfacial hydrogen-atom transfer toward the Co center and reacts with the newly adsorbed O_3 to form a second Co-OOOH intermediate. The decomposition of this Co-OOOH intermediate releases the second ·OOOH radical, which subsequently re-adsorbs onto Co centers to evolute the first O_2 molecule, while leaving bridging O atoms shared by neighboring Co sites. In view of the complexity of this step and its pivotal role in the overall catalytic cycle, its kinetics were explicitly evaluated. The elementary step in which the *OOOH

ARTICLE IN PRESS

intermediate forms the first O_2 molecule and *OH (TS1), as well as the subsequent transfer of the resulting *OH (TS2), was calculated. According to the DFT results, the Gibbs free energy barrier (TS1) for the formation of $*O_2$ and *OH intermediates from *OOOH is 0.47 eV, and the barrier for the transfer of the generated *OH to the O atom of Fe-O-Co (TS2) is 0.64 eV. These DFT-calculated energy barriers are moderate, indicating that the reaction process is kinetically feasible. Finally, the transient Co-OOH intermediate decomposes to release the third O_2 molecule, after which both hydrogen atoms return to the Fe site to reconstitute the coordinated water. Overall, the key driving force of the O_3 catalytic decomposition process on Co_3O_4@PCN-333(Fe) is hydrogen-atom transfer mechanism (Tables S3-S4 and Fig. S20), in which hydrogen atoms was transferred among the Fe_3O cluster, the interfacial oxygen and the Co sites, ensuring continuous regeneration of active centers. In addition, the O_2 desorption barrier on bare Co_3O_4 was also calculated and found to be 1.84 eV (Fig. S21), which is much higher than the corresponding value of 0.62 eV on Co_3O_4@PCN-333(Fe), underscoring the advantage of the hydrogen-atom transfer nanoreactor. The above results indicated that the hydrogen-atom transfer between the interface between Co_3O_4 and Fe_3O cluster enable stepwise O_3 activation, efficient O_2 release, and accelerated active-site regeneration, thereby accounting for the high catalytic activity observed experimentally.

ARTICLE IN PRESS

Discussion

In conclusion, we have successfully constructed a hydrogen-atom transfer nanoreactor by encapsulating ultrafine metal oxides (UMOs) within the nanopores of an Fe-based metal-organic framework, PCN-333(Fe). Among the encapsulated architectures, 30% Co_3O_4@PCN-333(Fe) maintains high and stable O_3 decomposition activity across a broad range of humidity levels, demonstrating its strong potential for practical applications in real-world environments. The outstanding O_3 decomposition performance is attributed to a hydrogen-atom transfer mechanism

ARTICLE IN PRESS

between the Co_3O_4 and Fe_3O of PCN-333 interfaces, which facilitates stepwise activation of O_3, promotes efficient O_2 release, and accelerates the regeneration of active sites. These findings underscore the significant potential of MOF-confined metal oxide materials in pollution control and may open new avenues for the development of advanced catalysts for O_3 decomposition.

Methods

Materials and reagents

$Co(NO_3)_2 \cdot 6H_2O$, $Ni(NO_3)_2 \cdot 6H_2O$, $MnSO_4$, $(NH_4)_2S_2O_8$, $CO(NH_2)_2$, $FeCl_3 \cdot 6H_2O$, and 2,4,6-Tris(carboxyphenyl)-1,3,5-triazine (H_3TATB) were purchased from Shanghai Macklin Biochemical Technology Co., Ltd. DMF, EtOH, Acetone was purchased from Shenyang Xinhua Reagent Factory without further purification.

The ozone (O_3) catalyst performance test system is self-made, and its main accessories are as follows: UV lamp and ballast were bought from Beijing Aerospace Hongda Optoelectronic Technology Co., Ltd. Ozone monitor (Model 202) was bought from 2B Technologies. Humidity generator was bought from Shanghai Penghe electronic technology Co., Ltd. Air pump (SPB-3) was bought from Beijing BCHP Analytical Technology Institute. Gas mass flowmeter (PIPG-M102-01-2000) was bought from Shaanxi Yidu Intelligence Technology Co., Ltd.

Synthesis of PCN-333(Fe)

PCN-333(Fe) was synthesized according to the previously reported literature[24]. H_3TATB (50 mg) and anhydrous $FeCl_3$ (60 mg) were dissolved in 10 mL of DMF, followed by the addition of 0.5

ARTICLE IN PRESS

mL trifluoroacetic acid. The resulting solution was transferred to a Teflon-lined autoclave and heated at 150 °C for 12 h, yielding a brown precipitate. After centrifugation, the product was repeatedly washed with fresh DMF and Acetone to remove any residual reactants.

Synthesis of UMOs@PCN-333(Fe)

Co_3O_4 precursor solution: dissolve 600 mg cobalt(II) nitrate hexahydrate ($Co(NO_3)_2 \cdot 6H_2O$) and 600 mg urea ($CO(NH_2)_2$) in 1 mL deionized water, then sonicate until completely dissolved.

NiO precursor solution: dissolve 600 mg nickel(II) nitrate hexahydrate ($Ni(NO_3)_2 \cdot 6H_2O$) and 600 mg urea ($CO(NH_2)_2$) in 1 mL deionized water, then sonicate until completely dissolved.

UMOs@PCN-333(Fe) hybrids were prepared by a sonication–microwave confinement strategy. Activated PCN-333(Fe) (50 mg) was ultrasonicated (15 min) in 20 mL anhydrous DMF to fully expose its hierarchical meso- and micro-pores. Separately, 1 mL UMOs precursor solution (Co_3O_4 or NiO precursor solution) was added dropwise to the MOF dispersion under continuous stirring. The mixture was aged at 0°C for 2 h to allow precursor diffusion and anchoring within the cavities. Subsequent microwave irradiation induced rapid in-situ nucleation of ultrafine Co_3O_4, or NiO clusters without disrupting the framework. After cooling, the product was collected by filtration, washed repeatedly with DMF and ethanol, and vacuum-dried at 80°C to furnish the corresponding UMOs@PCN-333(Fe) composite.

Synthesis of Co_3O_4

The Co_3O_4 precursor solution was prepared by dissolving 30 mg of cobalt(II) nitrate hexahydrate

ARTICLE IN PRESS

($Co(NO_3)_2 \cdot 6H_2O$) and 31 mg of urea ($CO(NH_2)_2$) in 50 μL of deionized water. The resulting mixture was subjected to microwave irradiation for a duration of 5 minutes to facilitate the reaction. After cooling to room temperature, the resulting powder was washed by H_2O and ethanol for 3 times, respectively. Finally, the product was dry at 85°C for 12 hrs.

Synthesis of NiO

The NiO precursor solution was prepared by dissolving 30 mg of nickel(II) nitrate hexahydrate ($Ni(NO_3)_2 \cdot 6H_2O$) and 31 mg of urea ($CO(NH_2)_2$) in 50 μL of deionized water. The resulting mixture was subjected to microwave irradiation for a duration of 5 minutes to facilitate the reaction. After cooling to room temperature, the resulting powder was washed by H_2O and ethanol for 3 times, respectively. Finally, the product was dry at 85°C for 12 hrs.

Structure characterization

The powder X-ray diffraction (PXRD) patterns were recorded on a Bruker Advanced D8 X-ray Powder Diffractometer (λ = 1.54056 Å). N_2 adsorption/desorption isotherms were measured by using a Beishide 3H-2000PS2 Surface Characterization Analyzer at 77 K. An Thermo Fisher 5700 Fourier transform infrared spectrometer was used for recording Fourier transform infrared (FT-IR) spectra. X-ray photoelectron spectroscopy (XPS) measurements were carried out using an ESCALAB 250 instrument. Metal oxides contents of all catalysts were determined by ICP-OES on an Agilent 5110(OES) atomic emission spectrometer. Raman spectra was recorded on Renishaw inVia™ InSpect Raman system. Synchrotron-based X-ray absorption spectroscopy (XAS)

ARTICLE IN PRESS

measurements, including XANES and EXAFS, were carried out at the BL14W1 beamline of the Shanghai Synchrotron Radiation Facility (SSRF) operated at 3.5 GeV with a maximum current of 260 mA. Powdered samples were uniformly spread on Kapton tape and mounted in a liquid-nitrogen-cooled cryostat (80 K) to minimize radiation damage. Spectra were collected in transmission mode for the Co K-edge (7709 eV) and Fe K-edge (7112 eV), with energy calibration performed simultaneously using Co and Fe metal foils as references. Data reduction and analysis were performed with Athena and Artemis software packages following standard procedures. Aberration-corrected high-resolution transmission electron microscopy (AC-HRTEM) and high-angle annular dark-field scanning transmission electron microscopy (HAADF-STEM) were performed on a JEOL JEM-ARM300F Grand ARM double-Cs-corrected microscope operated at 300 kV (JEOL Ltd., Japan). Powder samples were ultrasonically dispersed in ethanol, drop-cast onto a holey carbon-coated copper grid, and dried under ambient conditions before imaging.

ARTICLE IN PRESS

O_3 decomposition test

The O_3 catalytic decomposition of UMOs@PCN-333(Fe) were evaluated through a homemade O_3 analysis system at room temperature. O_3 was generated from compressed air manufactured from a fully automatic air source (SPB-3, Beijing BCHP Analytical Technology Institute) by an ultraviolet lamp (10-08100, Beijing UVCN). Before the test, all samples were vacuum-dried at 120°C for 12 hours to remove guest molecules from the structure. Then, the mixture of the 50 mg catalysts and 450 mg of quartz sand were loaded into the quartz tube reactor. The total inlet gas flow was kept

ARTICLE IN PRESS

at 1000 mL/min, and the inlet O_3 concentration was kept at 40 ± 1 ppm; the concentration of O_3 and RH were controlled by controlling the flow of blank air and O_3 while the total gas flow remained unchanged. The inlet and outlet O_3 concentration as well as RH were measured by an O_3 detector (model 202, 2B Technologies) and a humidity and temperature meter. The O_3 conversion rate was calculated via the following formula:

$$O_3 \text{ conversion } (\%) = (C_{inlet} - C_{outlet}) / C_{inlet} \times 100\% \quad (1)$$

where C_{inlet} and C_{outlet} are inlet and outlet concentrations of O_3, respectively.

Computational details

All DFT calculations were carried out using the CP2K code (V2024.1)[45]. The Gaussian-and-plane-wave (GPW) scheme was employed. Core electrons were described by norm-conserving Goedecker–Teter–Hutter (GTH) pseudopotentials[46-48], and the valence electron wavefunctions were expanded in double-ζ Gaussian basis sets with polarization functions[49], together with an auxiliary plane-wave basis set with a kinetic energy cutoff of 450 Ry. Exchange–correlation effects were treated within the generalized-gradient approximation using the Perdew-Burke-Ernzerhof (PBE) functional[50]. Geometry optimizations were performed with the Broyden-Fletcher-Goldfarb-Shanno (BFGS) algorithm until the self-consistent-field (SCF) energy converged to 1.0×10^{-6} a.u. Long-range van der Waals interactions between the adsorbates and the framework were accounted for using the DFT-D3 dispersion correction with an empirical damping function[51]. For Fe- and Co-containing models, the total spin multiplicities were set to 4 and 3, respectively. All calculations

ARTICLE IN PRESS

were carried out in a cubic simulation cell of 35 × 35 × 35 $Å^3$.

The Gibbs free energy change for each elementary step was calculated at 298.15 K, defining as follows:

$$\Delta G = \Delta E_{DFT} + \Delta E_{ZPE} - T\Delta S \quad (2)$$

where ΔE is the difference of electronic energy calculated with CP2K, ΔE_{ZPE} is the difference of zero-point energy (ZEP), and $T\Delta S$ is the changed entropy value. E_{ZPE} and TS were calculated using the following equations for each reaction intermediates,

$$E_{ZPE} = \frac{1}{2}\sum_i h\nu_i \quad (3)$$

$$TS = \sum_i h\nu_i \left(\frac{1}{e^{h\nu_i/k_BT}}\right) - k_BT\sum_i \ln\left(1 - e^{-h\nu_i/k_BT}\right) \quad (4)$$

where h, ν_i, and k_B are Planck's constant, vibrational frequencies, and Boltzmann constant, respectively. For vibrational frequency calculations, only the adsorbates were included with negligible contributions from the framework of the catalyst.

The Gibbs free energy of O_3 or reaction species adsorbed on the substrates was obtained after the geometry optimization for the adsorption and reaction process. And then, the Gibbs free energy change (ΔG) was calculated between the free energy for each reaction step.

Data Availability

All data supporting the findings of this study are available within the article and its Supplementary Information, or from the corresponding author upon reasonable request. Source Data are provided with the paper.

ARTICLE IN PRESS

References

1. Yeung LY*, et al.* Isotopic Constraint on the Twentieth-Century Increase in Tropospheric Ozone. *Nature* **570**, 224-227 (2019).
2. Zhao Y*, et al.* Air Pollution Modulates Trends and Variability of the Global Methane Budget. *Nature* **642**, 369-375 (2025).
3. Finlayson-Pitts BJ*, et al.* Tropospheric Air Pollution: Ozone, Airborne Toxics, Polycyclic Aromatic Hydrocarbons, and Particles. *Science* **276**, 1045-1051 (1997).
4. Wang N*, et al.* Typhoon-Boosted Biogenic Emission Aggravates Cross-Regional Ozone Pollution in China. *Sci. Adv.* **8**, eabl6166.
5. Feng Z*, et al.* Ozone Pollution Threatens the Production of Major Staple Crops in East Asia. *Nat. Food* **3**, 47-56 (2022).
6. Achebak H*, et al.* Geographic Sources of Ozone Air Pollution and Mortality Burden in Europe. *Nat. Med.* **30**, 1732-1738 (2024).
7. Simpkins G. Ozone Damage Costs Billions. *Nat. Rev. Earth Environ.* **3**, 102-102 (2022).
8. Li X*, et al.* Recent Advances in Catalytic Decomposition of Ozone. *J. Environ. Sci.* **94**, 14-31 (2020).
9. Zhu Y*, et al.* Rapid Ozone Decomposition over Water-activated Monolithic MoO_3/Graphdiyne Nanowalls under High Humidity. *Angew. Chem., Int. Ed.* **62**, e202309158 (2023).
10. Yang J*, et al.* Defect-Based Lewis Pairs on Hydrophobic MnO Mesocrystals for Robust and Efficient Ozone Decomposition. *Nat. Commun.* **16**, 2922-2930 (2025).

ARTICLE IN PRESS

ARTICLE IN PRESS

11. Dai W*, et al.* Exceptional Ozone Decomposition over δ-MnO_2/AC under An Entire Humidity Environment. *Environ. Sci. Technol.* **57**, 17727-17736 (2023).

12. Deng H*, et al.* Role of Structural Defects in MnOx Promoted by Ag Doping in the Catalytic Combustion of Volatile Organic Compounds and Ambient Decomposition of O3. *Environ. Sci. Technol.* **53**, 10871-10879 (2019).

13. Gong S*, et al.* Heterostructured Ni/NiO Nanocatalysts for Ozone Decomposition. *ACS Appl. Nano Mater.* **3**, 597-607 (2019).

14. Zhu G*, et al.* Encapsulate α-MnO_2 Nanofiber within Graphene Layer to Tune Surface Electronic Structure for Efficient Ozone Decomposition. *Nat. Commun.* **12**, 4152-4161 (2021).

15. Han Y*, et al.* Topology-directed cage engineering in MOFs for Efficient $C_2H_2/CO_2/C_2H_4$ separation. *J. Am. Chem. Soc.* **147**, 19262-19271 (2025).

16. Wen L*, et al.* Electronic State and Microenvironment Modulation of Metal Nanoparticles Stabilized by MOFs for Boosting Electrocatalytic Nitrogen Reduction. *Adv. Mater.* **35**, 2210669-2210676 (2023).

17. Feng D*, et al.* Zirconium-Metalloporphyrin PCN-222: Mesoporous Metal-Organic Frameworks with Ultrahigh Stability as Biomimetic Catalysts. *Angew. Chem., Int. Ed.* **51**, 10307-10310 (2012).

18. Hu S*, et al.* Selectivity Control in the Direct CO Esterification over Pd@UiO-66: The Pd Location Matters. *Angew. Chem., Int. Ed.*, e202311625 (2023).

19. Ling L-L*, et al.* Light-Assisted CO_2 Hydrogenation over Pd_3Cu@UiO-66 Promoted by Active

ARTICLE IN PRESS

Sites in Close Proximity. *Angew. Chem., Int. Ed.* **61**, e202116396 (2022).

20. Ko S*, et al.* Mesoporous CuO Particles Threaded with CNTs for High-Performance Lithium-Ion Battery Anodes. *Adv. Mater.* **24**, 4451-4456 (2012).
21. Kwon HJ*, et al.* Large-Scale Synthesis and Medical Applications of Uniform-Sized Metal Oxide Nanoparticles. *Adv. Mater.* **30**, 1704290-1704313 (2018).
22. Zhou T*, et al.* Ultrafine Metal Nanoparticles Isolated on Oxide Nano-Islands as Exceptional Sintering-Resistant Catalysts. *Nat. Mater.* **24**, 891-899 (2025).
23. Qiao G-Y*, et al.* Perovskite Quantum Dots Encapsulated in a Mesoporous Metal-Organic Framework as Synergistic Photocathode Materials. *J. Am. Chem. Soc.* **143**, 14253-14260 (2021).
24. Feng D*, et al.* Stable Metal-Organic Frameworks Containing Single-Molecule Traps for Enzyme Encapsulation. *Nat. Commun.* **6**, 5979-5986 (2015).
25. Jiang Z*, et al.* Filling Metal-Organic Framework Mesopores with TiO_2 for CO_2 Photoreduction. *Nature* **586**, 549-554 (2020).
26. Wang X*, et al.* Atomic-Scale Insights into Surface Lattice Oxygen Activation at the Spinel/Perovskite interface of $Co_3O_4/La_{0.3}Sr_{0.7}CoO_3$. *Angew. Chem., Int. Ed.* **58**, 11720-11725 (2019).
27. Wan W*, et al.* Carbon-Supported Single Fe/Co/Ni Atom Catalysts for Water Oxidation: Unveiling the Dynamic Active Sites. *Angew. Chem., Int. Ed.* **64**, e202424629 (2025).
28. Kim M*, et al.* Reducing the Barrier Energy of Self-Reconstruction for Anchored Cobalt

ARTICLE IN PRESS

Nanoparticles as Highly Active Oxygen Evolution Electrocatalyst. *Adv. Mater.* **31**, 1901977-1901984 (2019).

29. Aijaz A, *et al.* Immobilizing highly catalytically active pt nanoparticles inside the pores of metal-organic framework: A double solvents approach. *J. Am. Chem. Soc.* **134**, 13926-13929 (2012).
30. Liu J, *et al.* In Situ Synthesis of Highly Dispersed and Ultrafine Metal Nanoparticles from Chalcogels. *J. Am. Chem. Soc.* **139**, 2900-2903 (2017).
31. Xie Y, *et al.* Modulation in Spin State of Co_3O_4 Decorated Fe Single Atom Enables a Superior Rechargeable Zinc-Air Battery Performance. *Adv. Mater.* **37**, 2414801-2414810 (2025).
32. Qian J, *et al.* Enhanced Stability and Narrowed D-Band Gap of Ce-Doped Co_3O_4 for Rechargeable Aqueous Zn-Air Battery. *Adv. Funct. Mater.* **33**, 2212021-2212029 (2023).
33. Wang H, *et al.* An Iron-Containing Metal-Organic Framework as A Highly Efficient Catalyst for Ozone Decomposition. *Angew. Chem., Int. Ed.* **57**, 16416-16420 (2018).
34. Sun ZB, *et al.* Ozone Decomposition by a Manganese-Organic Framework over the Entire Humidity Range. *J. Am. Chem. Soc.* **143**, 5150-5157 (2021).
35. Dong C, *et al.* Catalytic Ozone Decomposition and Adsorptive VOCs Removal in Bimetallic Metal-Organic Frameworks. *Nat. Commun.* **13**, 4991-5000 (2022).
36. Wang Z, *et al.* Layered Double Hydroxide Catalysts for Ozone Decomposition: The Synergic Role of M^{2+} and M^{3+}. *Environ. Sci. Technol.* **56**, 1386-1394 (2022).
37. Li X, *et al.* Oxygen Vacancies Induced by Transition Metal Doping in γ-MnO_2 for Highly

ARTICLE IN PRESS

Efficient Ozone Decomposition. *Environ. Sci. Technol.* **52**, 12685-12696 (2018).

38. Wan X*, et al.* Ozone Decomposition below Room Temperature Using Mn-based Mullite YMn_2O_5. *Environ. Sci. Technol.* **56**, 8746-8755 (2022).
39. Li X*, et al.* Regulating the Chemical State of Silver via Surface Hydroxyl Groups to Enhance Ozone Decomposition Performance of Ag/Fe_2O_3 Catalyst. *Catal. Today* **410**, 117-126 (2023).
40. Valdés H*, et al.* New Insight of the Influence of Acidic Surface Sites of Zeolite on the Ability to Remove Gaseous Ozone Using Operando DRIFTS Studies. *Micropor. Mesopor. Mat.* **294**, 109912-109922 (2020).
41. Liang X*, et al.* Mesoporous Poorly Crystalline α-Fe_2O_3 with Abundant Oxygen Vacancies and Acid Sites for Ozone Decomposition. *Sci. Total Environ.* **804**, 150161-150172 (2022).
42. Jing C*, et al.* Electrocatalyst with Dynamic Formation of the Dual-Active Site from the Dual Pathway Observed by In Situ Raman Spectroscopy. *ACS Catal.* **12**, 10276-10284 (2022).
43. Bo X*, et al.* Operando Raman Spectroscopy Reveals Cr-Induced-Phase Reconstruction of NiFe and CoFe Oxyhydroxides for Enhanced Electrocatalytic Water Oxidation. *Chem. Mater.* **32**, 4303-4311 (2020).
44. Niu S*, et al.* Cu Regulating the Bifunctional Activity of Co-O Sites for the High-Performance Rechargeable Zinc-Air Battery. *ACS Appl. Mater. Interfaces* **16**, 36295-36303 (2024).
45. VandeVondele J*, et al.* Quickstep: Fast and accurate density functional calculations using a mixed Gaussian and plane waves approach. *Comput. Phys. Commun.* **167**, 103-128 (2005).
46. Goedecker S*, et al.* Separable dual-space Gaussian pseudopotentials. *Phys. Rev. B* **54**, 1703-

ARTICLE IN PRESS

1710 (1996).

47. Hartwigsen C*, et al.* Relativistic separable dual-space Gaussian pseudopotentials from H to Rn. *Phys. Rev. B* **58**, 3641-3662 (1998).
48. Krack M*, et al.* All-electron ab-initio molecular dynamics. *Physical Chemistry Chemical Physics* **2**, 2105-2112 (2000).
49. VandeVondele J*, et al.* Gaussian basis sets for accurate calculations on molecular systems in gas and condensed phases. *J. Chem. phys.* **127**, 114105 (2007).
50. Perdew JP*, et al.* Generalized Gradient Approximation Made Simple. *Phys. Rev. Lett.* **77**, 3865-3868 (1996).
51. Grimme S*, et al.* A consistent and accurate ab initio parametrization of density functional dispersion correction (DFT-D) for the 94 elements H-Pu. *J. Chem. phys.* **132**, 154104 (2010).

ARTICLE IN PRESS

Acknowledgments

This work was supported by the National Natural Science Foundation of China (22171121), the Applied Basic Research Plan of Liaoning Province (2023JH2/101300007).

Author contributions

Z.H conceived and designed this project. Y.L and T.L performed the experiments, Y.L and Y.H carried out the DFT calculation, Y.L analyzed the data, Y.L, Z.H and Z.-M.Z wrote and revised the manuscript.

Competing interests statement

The authors declare no competing interests.

ARTICLE IN PRESS

Figure Captions

Fig. 1. Synthetic methodology for UMOs@PCN-333(Fe) via a sonication-microwave confinement strategy. Metal oxide precursor loading and immobilization inside PCN-333(Fe) are followed by confined conversion to ultrafine metal oxides, yielding robust hybrids.

Fig. 2. AC-HAADF-STEM of 30% Co_3O_4@PCN-333(Fe) and pristine PCN-333(Fe). (a) HAADF-STEM image of pristine PCN-333(Fe). **(b)** HAADF-STEM overview and **(c)** magnified view of 30% Co_3O_4@PCN-333(Fe). Insets highlight the mesoporous arrangement of PCN-333 viewed along the (110) crystallographic plane.

Fig. 3. Structural and textural characterization of Co_3O_4@PCN-333(Fe) with varying Co_3O_4 loadings. (a) Co K-edge XANES spectra, **(b)** corresponding FT-EXAFS spectra, and **(c)** FT-EXAFS fitting curve of 30% Co_3O_4@PCN-333(Fe). **(d)** PXRD patterns of Co_3O_4@PCN-333(Fe) with various and Co_3O_4 contents. **(e)** Raman spectra of 30% Co_3O_4@PCN-333(Fe). **(f)** N_2 adsorption isotherm of Co_3O_4@PCN-333(Fe) with various and Co_3O_4 contents.

Fig. 4. O_3 decomposition performance of various catalysts under different conditions. (a) 30% Co_3O_4@PCN-333(Fe) under 10-90% RH at 40°C. **(b)** Comparison among 30% Co_3O_4@PCN-333(Fe), pure Co_3O_4, and PCN-333(Fe) under 10% RH at 40°C. **(c)** Comparison among 30% Co_3O_4@PCN-333(Fe), pure Co_3O_4, and PCN-333(Fe) under 90% RH at 40°C. **(d)** O_3 conversion

ARTICLE IN PRESS

over Co_3O_4@PCN-333(Fe) with different Co_3O_4 loadings. **(e)** Performance of 30% Co_3O_4@PCN-333(Fe) under alternating humidity (30-90% RH) at 40°C. **(f)** Performance of 30% Co_3O_4@PCN-333(Fe) under alternating temperature (10-40°C). **(g)** Performance of 30% Co_3O_4@PCN-333(Fe) across 10-40 °C. **(h)** O_3 conversion of 30% Co_3O_4@PCN-333(Fe) under simulated Yangtze River Delta region environmental conditions. **(i)** Comparison of O_3 conversion among three different UMOs@PCN-333(Fe) composites.

Fig. 5. Surface chemical states and structural evolution of 30% Co_3O_4@PCN-333(Fe) under O_3 exposure. XPS spectra of **(a)** Co 2*p* and **(b)** Fe 2*p* of 30% Co_3O_4@PCN-333(Fe) and other reference materials. **(c)** in situ DRIFT spectra and **(d)** in situ Raman spectra of 30% Co_3O_4@PCN-333(Fe) with continuous O_3 flow at room temperature.

Fig. 6. Proposed catalytic mechanism of O_3 decomposition on Co_3O_4@PCN-333(Fe). (a) the adsorption sites of H_2O and O_3 on Co_3O_4@PCN-333(Fe), **(b)** the reaction pathways and **(c)** stationary-point structures for O_3 decomposition catalyzed by Co_3O_4@PCN-333(Fe). Fe atoms are light purple, Co atoms are light blue, O atoms are red, and H atoms are white.

Editorial summary:

Ground-level ozone is harmful, and efficient removal in humid air remains difficult. Ultrafine

ARTICLE IN PRESS

cobalt oxide confined in a metal-organic framework delivers sustained complete conversion across wide humidity by enabling interfacial hydrogen transfer.

Peer review information: *Nature Communications* thanks Yongfa Zhu, and the other, anonymous, reviewer(s) for their contribution to the peer review of this work. A peer review file is available.

ARTICLE IN PRESS

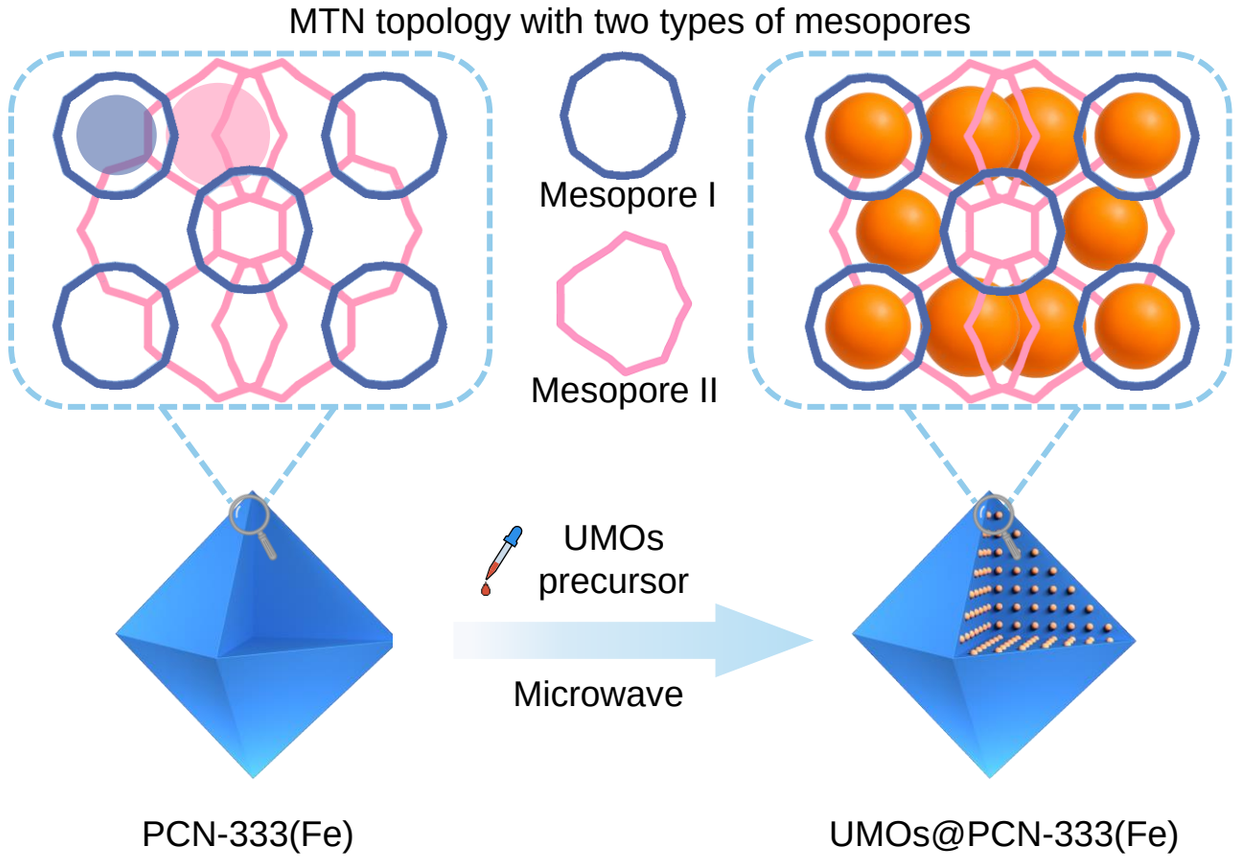
MTN topology with two types of mesopores
Mesopore I
Mesopore II
UMOs
precursor
Microwave
PCN-333(Fe)
UMOs@PCN-333(Fe)

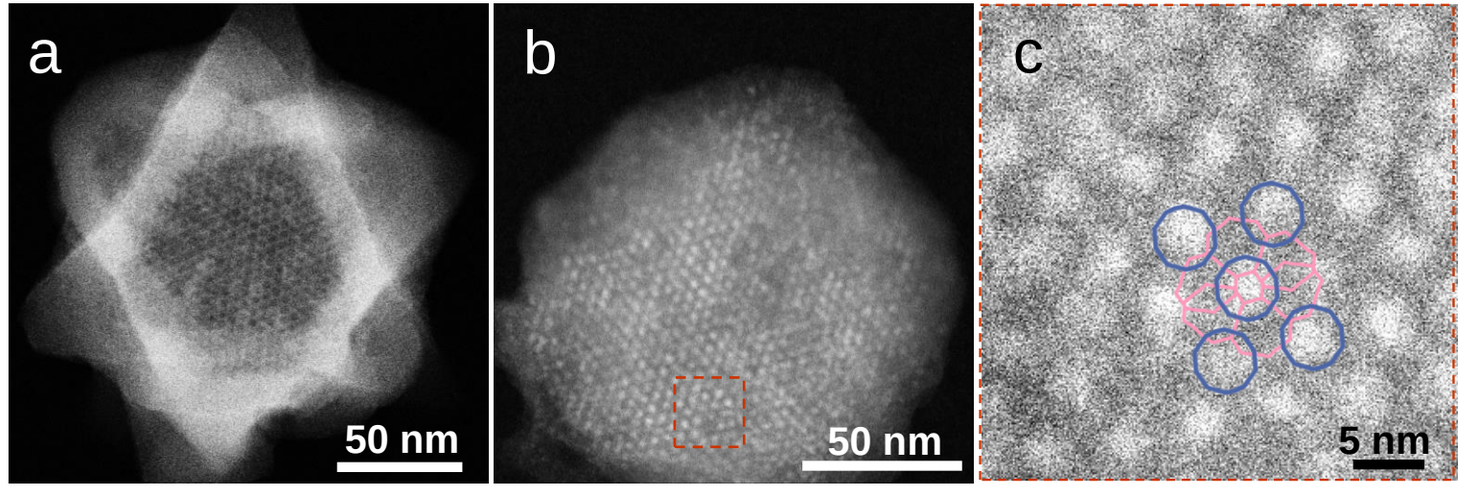
a
50 nm
b
50 nm
c
5 nm

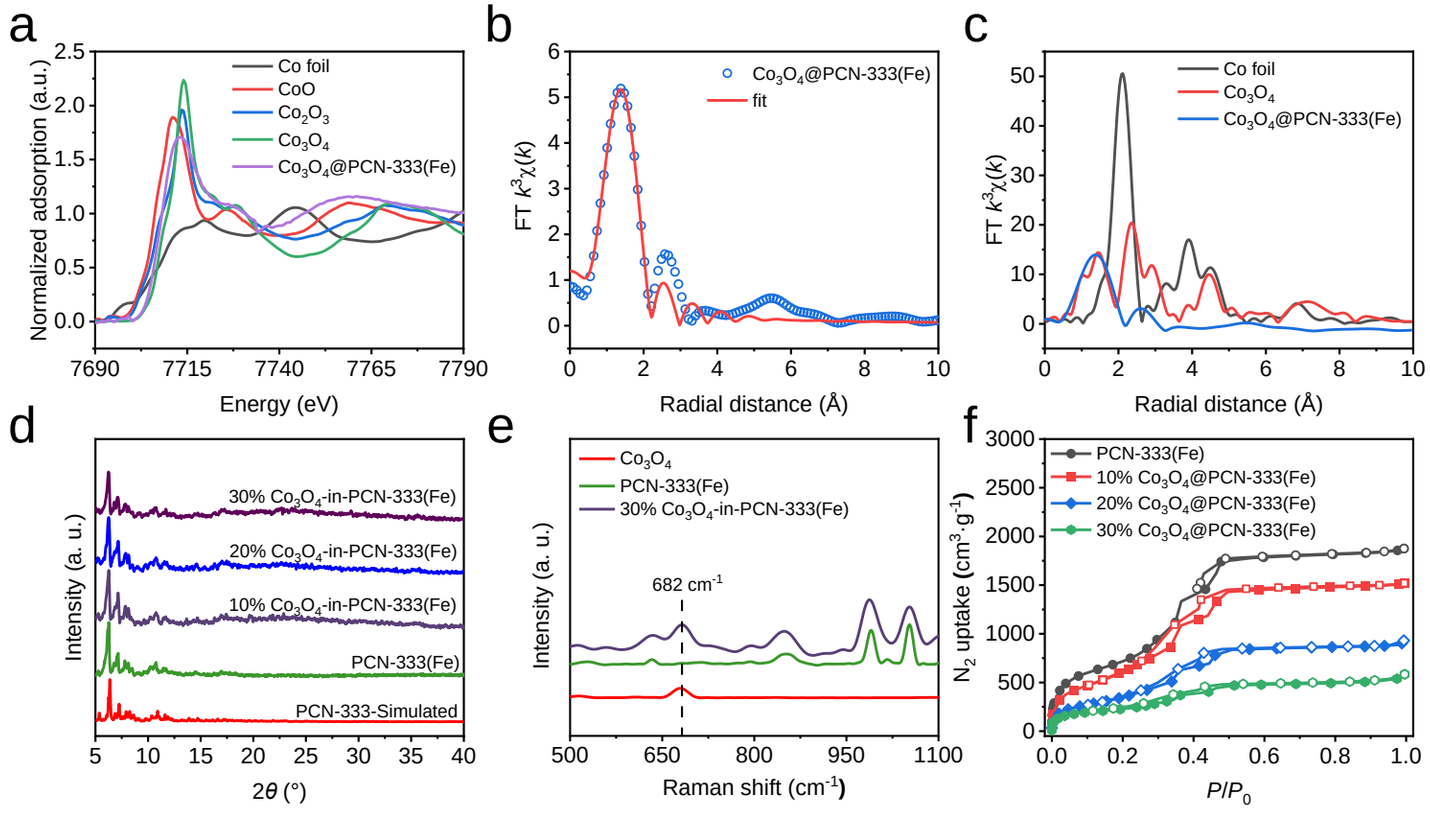
a
Normalized adsorption (a.u.)
Energy (eV)
Co foil
CoO
Co2O3
Co3O4
Co3O4@PCN-333(Fe)
b
FT k3χ(k)
Radial distance (Å)
Co3O4@PCN-333(Fe)
fit
c
FT k3χ(k)
Radial distance (Å)
Co foil
Co3O4
Co3O4@PCN-333(Fe)
d
Intensity (a. u.)
2θ (°)
30% Co3O4-in-PCN-333(Fe)
20% Co3O4-in-PCN-333(Fe)
10% Co3O4-in-PCN-333(Fe)
PCN-333(Fe)
PCN-333-Simulated
e
Intensity (a. u.)
Raman shift (cm-1)
Co3O4
PCN-333(Fe)
30% Co3O4-in-PCN-333(Fe)
682 cm-1
f
N2 uptake (cm3·g-1)
P/P0
PCN-333(Fe)
10% Co3O4@PCN-333(Fe)
20% Co3O4@PCN-333(Fe)
30% Co3O4@PCN-333(Fe)

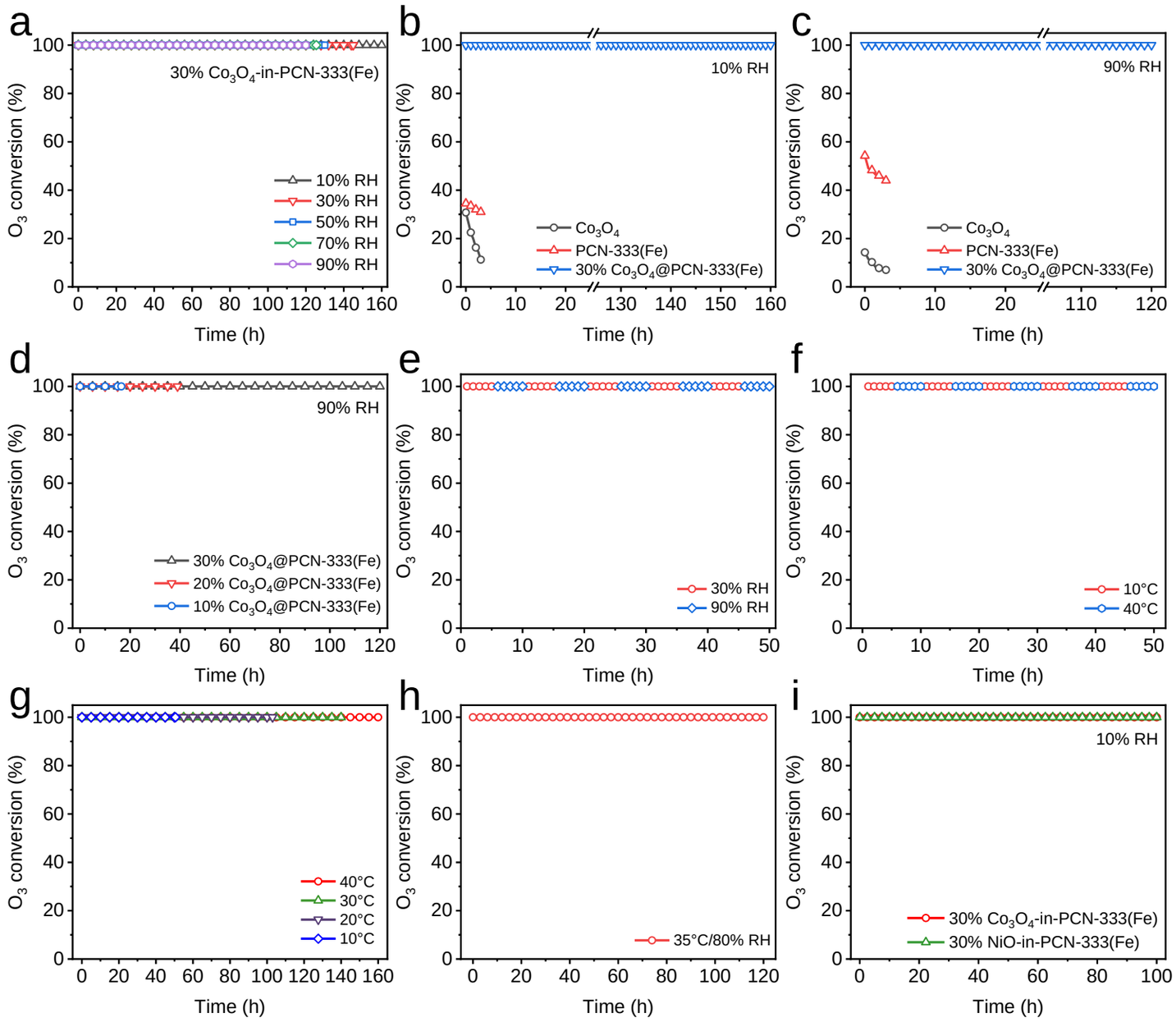
a
30% Co3O4-in-PCN-333(Fe)
10% RH
30% RH
50% RH
70% RH
90% RH
b
10% RH
Co3O4
PCN-333(Fe)
30% Co3O4@PCN-333(Fe)
c
90% RH
Co3O4
PCN-333(Fe)
30% Co3O4@PCN-333(Fe)
d
90% RH
30% Co3O4@PCN-333(Fe)
20% Co3O4@PCN-333(Fe)
10% Co3O4@PCN-333(Fe)
e
30% RH
90% RH
f
10°C
40°C
g
40°C
30°C
20°C
10°C
h
35°C/80% RH
i
10% RH
30% Co3O4-in-PCN-333(Fe)
30% NiO-in-PCN-333(Fe)
O3 conversion (%)
Time (h)

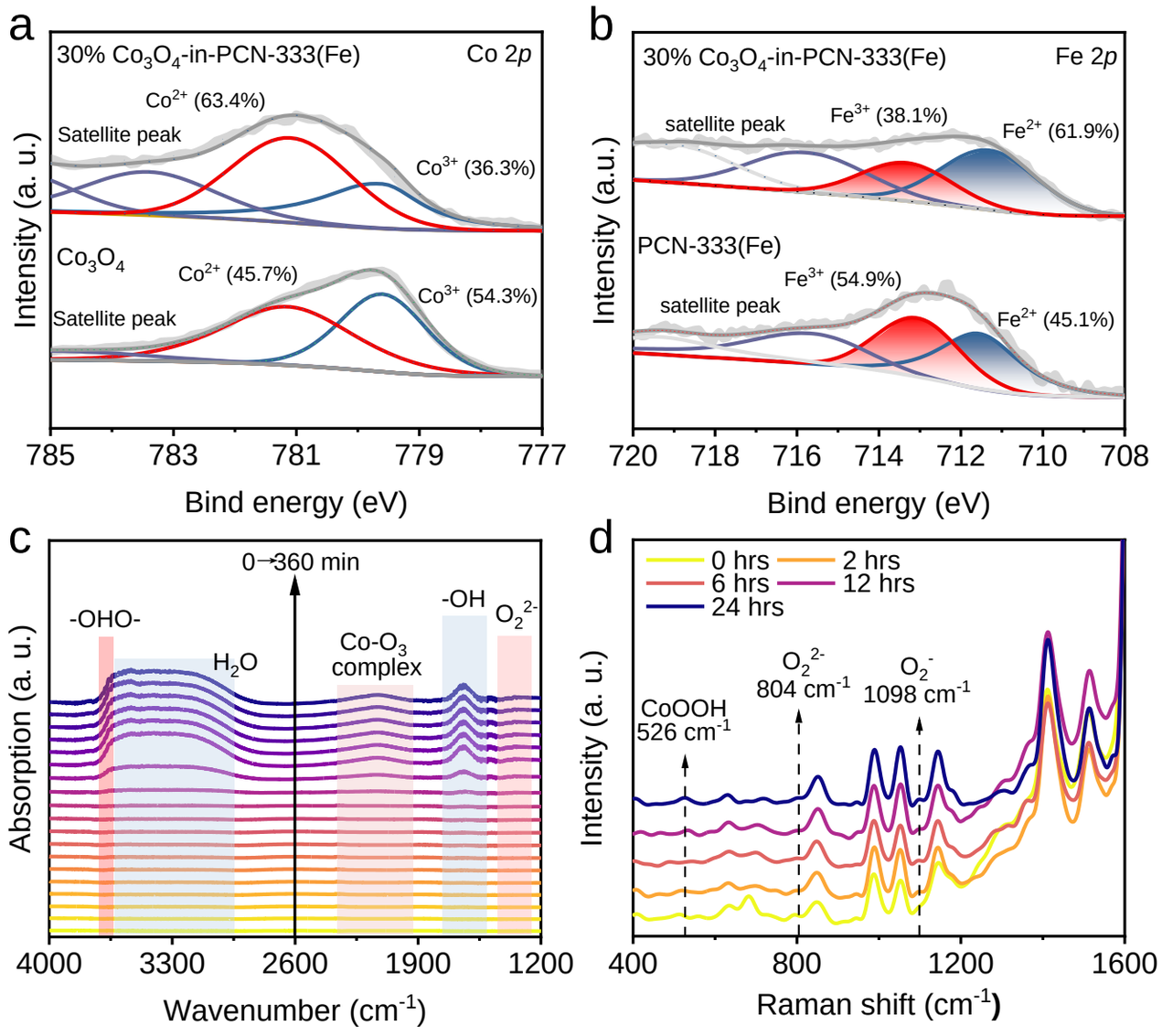
a
30% Co3O4-in-PCN-333(Fe)
Co 2p
Co2+ (63.4%)
Satellite peak
Co3+ (36.3%)
Co3O4
Co2+ (45.7%)
Satellite peak
Co3+ (54.3%)
Intensity (a. u.)
785
783
781
779
777
Bind energy (eV)
b
30% Co3O4-in-PCN-333(Fe)
Fe 2p
satellite peak
Fe3+ (38.1%)
Fe2+ (61.9%)
PCN-333(Fe)
Fe3+ (54.9%)
satellite peak
Fe2+ (45.1%)
Intensity (a.u.)
720
718
716
714
712
710
708
Bind energy (eV)
c
0→360 min
-OHO-
H2O
Co-O3 complex
-OH
O2 2-
Absorption (a. u.)
4000
3300
2600
1900
1200
Wavenumber (cm-1)
d
0 hrs
2 hrs
6 hrs
12 hrs
24 hrs
CoOOH
526 cm-1
O2 2-
804 cm-1
O2 -
1098 cm-1
Intensity (a. u.)
400
800
1200
1600
Raman shift (cm-1)

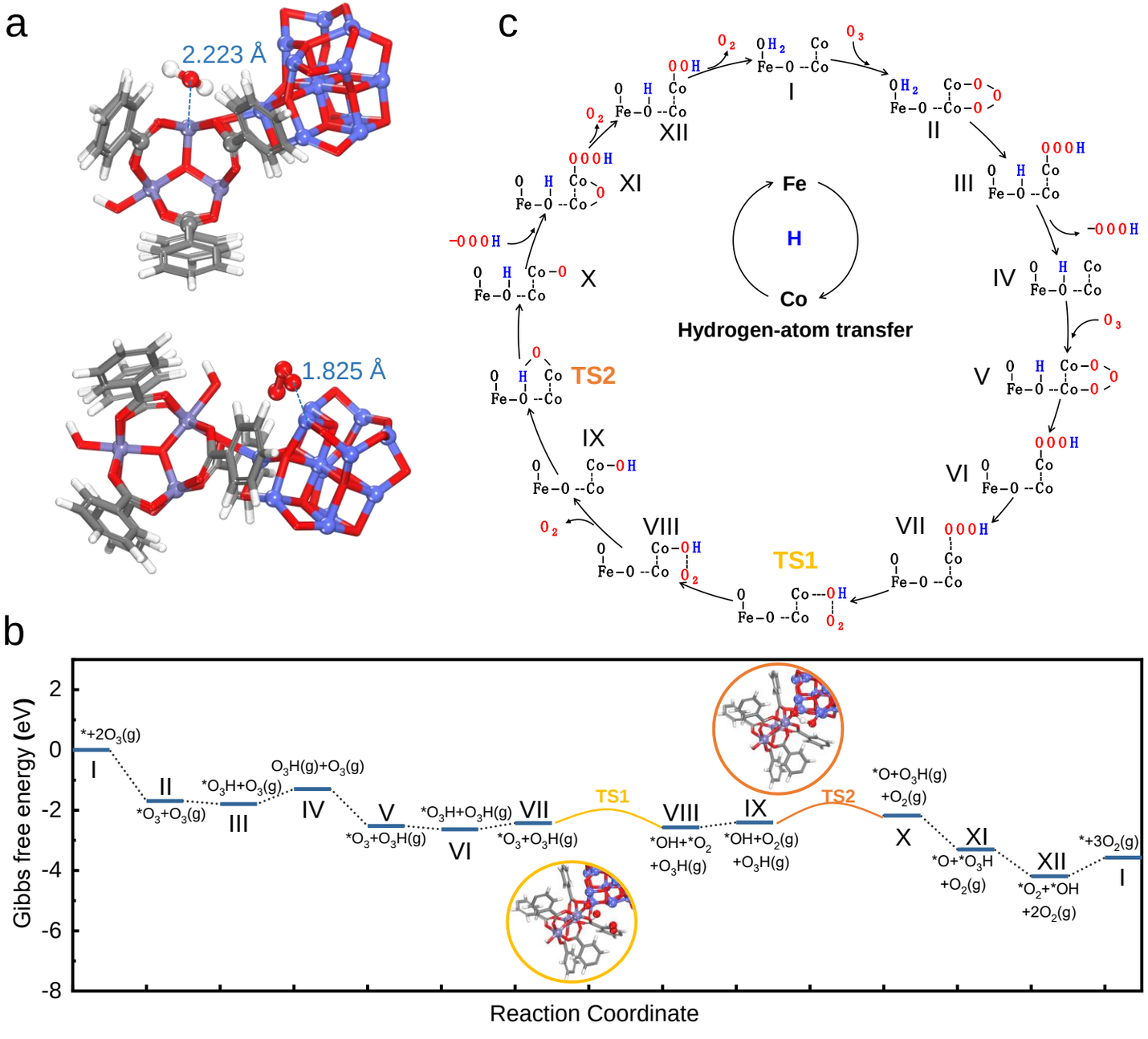
a
2.223 Å
1.825 Å
c
Fe
H
Co
Hydrogen-atom transfer
TS1
TS2
b
Gibbs free energy (eV)
Reaction Coordinate
*+2O3(g)
*O3+O3(g)
*O3H+O3(g)
O3H(g)+O3(g)
*O3+O3H(g)
*O3H+O3H(g)
*OH+*O2 +O3H(g)
*OH+O2(g) +O3H(g)
*O+O3H(g) +O2(g)
*O+*O3H +O2(g)
*O2+*OH +2O2(g)
*+3O2(g)